




Three-dimensional multiple-relaxation-time discrete Boltzmann model of compressible reactive flows with nonequilibrium effects

Cite as: AIP Advances 11, 045217 (2021); <https://doi.org/10.1063/5.0047480>

Submitted: 20 March 2021 . Accepted: 01 April 2021 . Published Online: 18 April 2021

 Yu Ji (吉雨),  Chuandong Lin (林传栋), and  Kai H. Luo (罗开红)



View Online



Export Citation



CrossMark

ARTICLES YOU MAY BE INTERESTED IN

[Double-D2Q9 lattice Boltzmann models with extended equilibrium for two-dimensional magnetohydrodynamic flows](#)

Physics of Fluids **33**, 035143 (2021); <https://doi.org/10.1063/5.0043998>

[A multiple-relaxation-time collision model for nonequilibrium flows](#)

Physics of Fluids **33**, 037134 (2021); <https://doi.org/10.1063/5.0046866>

[Extended lattice Boltzmann model for gas dynamics](#)

Physics of Fluids **33**, 046104 (2021); <https://doi.org/10.1063/5.0048029>

Call For Papers!

AIP Advances

SPECIAL TOPIC: Advances in
Low Dimensional and 2D Materials

Three-dimensional multiple-relaxation-time discrete Boltzmann model of compressible reactive flows with nonequilibrium effects

Cite as: AIP Advances 11, 045217 (2021); doi: 10.1063/5.0047480

Submitted: 20 March 2021 • Accepted: 1 April 2021 •

Published Online: 19 April 2021



View Online



Export Citation



CrossMark

Yu Ji (吉雨),¹ Chuandong Lin (林传栋),^{2,a)} and Kai H. Luo (罗开红)^{3,b)}

AFFILIATIONS

¹Center for Combustion Energy, Key Laboratory for Thermal Science and Power Engineering of Ministry of Education, Department of Energy and Power Engineering, Tsinghua University, Beijing 100084, China

²Sino-French Institute of Nuclear Engineering and Technology, Sun Yat-sen University, Zhuhai 519082, China

³Department of Mechanical Engineering, University College London, Torrington Place, London WC1E 7JE, United Kingdom

^{a)}Electronic mail: linchd3@mail.sysu.edu.cn

^{b)}Author to whom correspondence should be addressed: K.Luo@ucl.ac.uk

ABSTRACT

Based on the kinetic theory, a three-dimensional multiple-relaxation-time discrete Boltzmann model (DBM) is proposed for nonequilibrium compressible reactive flows where both the Prandtl number and specific heat ratio are freely adjustable. There are 30 kinetic moments of the discrete distribution functions, and an efficient three-dimensional thirty-velocity model is utilized. Through the Chapman–Enskog analysis, the reactive Navier–Stokes equations can be recovered from the DBM. Unlike existing lattice Boltzmann models for reactive flows, the hydrodynamic and thermodynamic fields are fully coupled in the DBM to simulate combustion in subsonic, supersonic, and potentially hypersonic flows. In addition, both hydrodynamic and thermodynamic nonequilibrium effects can be obtained and quantified handily in the evolution of the discrete Boltzmann equation. Several well-known benchmarks are adopted to validate the model, including chemical reactions in the free falling process, thermal Couette flow, one-dimensional steady or unsteady detonation, and a three-dimensional spherical explosion in an enclosed cube. It is shown that the proposed DBM has the capability to simulate both subsonic and supersonic fluid flows with or without chemical reactions.

© 2021 Author(s). All article content, except where otherwise noted, is licensed under a Creative Commons Attribution (CC BY) license (<http://creativecommons.org/licenses/by/4.0/>). <https://doi.org/10.1063/5.0047480>

I. INTRODUCTION

Reactive flows encompassing a wide variety of nonlinear, unsteady, and nonequilibrium processes are common in nature and industry.¹ In fact, more than four-fifths of mankind's utilized energy is generated from the exothermic reactive flows.² In the past few decades, considerable research has been devoted to reactive flows, including supersonic and hypersonic flows related to the supersonic aircraft, rocket engine, detonation engine, supersonic combustion ramjet, etc. However, there are still many problems that have not been solved due to the complex physical and chemical processes involved, such as high compressibility, strong flow discontinuity, and combustion instability. In addition, these processes are usually accompanied by the hydrodynamic and thermodynamic

nonequilibrium effects as well as the complex interplay between the chemical reaction and fluid flow. Moreover, these processes cover a wide range of spatial and temporal scales.^{3–6} In order to study the reactive flow in detail, experimental techniques have been widely used.^{7,8} However, experiments for supersonic and hypersonic reactive flows are difficult and expensive to conduct; and the measurements are usually global quantities only. On the other hand, numerical simulations provide a convenient tool for relevant research and become more and more reliable and cost-effective.

The supersonic reactive flow modeling approaches can generally be classified into three groups. The first group is the conventional simulation methods based on the continuum assumption, such as direct numerical simulation,⁹ large eddy simulation,¹⁰ and Reynolds-averaged Navier–Stokes (NS).¹¹ These conventional

methods are good at capturing the main hydrodynamic characteristics. However, they lack the ability to describe thermodynamic nonequilibrium effects under highly nonequibrated conditions, such as the shock or detonation front.^{12,13} The second group is the microscopic methods, like molecular dynamics.¹⁴ The molecular dynamics gets rid of the local equilibrium assumption and thus can be used to study the detailed hydrodynamic and thermodynamic properties.^{15–17} On the other hand, the computational cost of molecular dynamics is usually prohibitive and the computational domain is always limited. The third group is the kinetic method¹⁴ based on the Boltzmann equation, which removes the limit of the local equilibrium assumption. A kinetic method, the lattice Boltzmann method (LBM), simulates the evolution of probability distribution functions in a discretized phase-space, which can be related to macroscopic quantities by moment relationships. The LBM has been successfully applied to simulate a variety of complex flows,¹⁸ including reactive flows.^{19–36} Merits of the LBM include the algorithm simplicity and locality, which lead to excellent performance on parallel clusters.

The key to dealing with reactive flows in the LBM is how to describe the energy and species mass fractions by LB formulation and couple them consistently. Current LBM formulations for reactive flows can be divided into two categories. The first category is the hybrid method, in which the flow simulation is accomplished through the weakly compressible LBM solver, while the transport equations for energy and species are solved by a finite difference scheme. In 2000, Filippova and Hänel proposed an LBM for reacting flows at a low Mach number with variable density.^{20,21} Later, Hosseini *et al.* modified the LBM solver and successfully simulated premixed and non-premixed flames with a detailed thermo-chemical model.^{22,23} In 2020, Shu *et al.* developed a simplified sphere function-based gas-kinetic flux solver for compressible viscous reacting flows.³⁷ This model applies the finite volume method to discretize the multi-component NS equations and computes numerical flux at the cell interface by using local solution of the Boltzmann equation. Although these models can handle the variable density, they lose the simplicity and the parallel efficiency of the pure LBM scheme.²⁴ The other category is the pure LB formulation. In 1997, with the assumption of irreversible infinite fast chemistry reactions, Succi *et al.* adopted the conserved scalar approach to describe the temperature and concentration fields.¹⁹ Similarly, in 2002, Yamamoto *et al.* assumed that the temperature field does not affect the flow field and simulated diffusion flames with a double-distribution-function LBM where the flow, temperature, and species fields are represented by two sets of distribution functions.^{25,26} Later, Lee *et al.*²⁷ and Chen *et al.*^{28,29} also utilized the double-distribution-function LBM to solve the low Mach number flows. Instead of using two sets of distribution functions, in 2012, Prasinari *et al.* extended a consistent LBM³⁸ by introducing correction terms, recovering the third- and fourth-order moments, and describing the temperature field.³⁰ In conclusion, these pure models are all limited to low Mach number flows. However, for supersonic and hypersonic reactive flows, high compressibility is an important factor.

Briefly, the aforementioned LBMs mainly focus on low Mach number reactive flows, which cannot make the best of the kinetic theory. To establish an LBM for reactive flows possessing more kinetic information beyond the NS equations, the LBM should

be compressible, thermal, and, at the same time, coupling the chemical reaction naturally. In addition, the model should take hydrodynamic and thermodynamic nonequilibrium effects into consideration.

In recent years, the discrete Boltzmann method (DBM) has been constructed to model and simulate nonequilibrium systems, with various velocity and time-space discretization schemes.^{31–35,39} The DBM and LBM can be viewed as two distinctive classes of discrete numerical methods based on the Boltzmann equation. Despite sharing the same origin and some similarities, the objectives, numerical implementation, and capabilities of the LBM and DBM are different. Basically, the LBM aims to recover the macroscopic behaviors of the flow system and acts as an alternative method to the continuum-based Navier–Stokes solver. On the other hand, the DBM is a discrete Boltzmann equation solver that aims to keep some kinetic features that go beyond the macroscopic behaviors. Numerically, discretization in space, time, and particle velocities is inter-dependent in the LBM algorithm. In the DBM, however, discretization in space, time, and particle velocities is decoupled, which allows a variety of numerical methods to be applied. As a result, the LBM requires different models for different types of flows (e.g., incompressible, compressible, thermal, or reactive), while a uniformed DBM framework can simulate all types of flows. Moreover, the DBM can capture both hydrodynamic and thermodynamic nonequilibrium effects explicitly.

To some extent, the mathematical framework of the DBM is similar to the rational extended thermodynamics (RET), which is also capable of explaining nonequilibrium phenomena. The RET proposed by Ruggeri and Sugiyama^{40,41} is motivated by the Boltzmann equation. Different from the kinetic theory, the RET focuses on the relations of the moments and forms a hierarchy of the balance laws. To achieve the closure of the moments, the RET truncates the hierarchy by adding restrictions from the universal principle. In this respect, the RET theory still belongs to the continuum approach but is applicable to the nonequilibrium state. On the other hand, the DBM is a kinetic approach and possesses kinetic features beyond the macroscopic equations.

Since 2013, several DBMs for reactive flows have been proposed.^{31–35,39} In 2013, Yan *et al.* proposed the first DBM for combustion.³¹ Very recently, Lin *et al.* proposed a two-dimensional model for detonations and investigated the main features of the hydrodynamic and thermodynamic nonequilibrium effects.³⁶ However, these formulations are two-dimensional but realistic reactive flows are a three-dimensional (3D) phenomenon and some important patterns and structures cannot be obtained from two-dimensional models. In 2017, Gan *et al.* proposed a 3D DBM for compressible flows without reaction based on the single-relaxation-time Boltzmann equation, fixing the Prandtl number $Pr = 1$.⁴² In this work, we extend the model to 3D reactive flows and present a multiple-relaxation-time (MRT) method to make the Prandtl number adjustable. Moreover, the hydrodynamic and thermodynamic nonequilibrium effects can be investigated to study the nonequilibrium behaviors.

The rest of this paper is organized as follows: In Sec. II, we formulate a 3D MRT DBM for reactive flows based on a three-dimensional thirty-velocity (D3V30) model. Through the Chapman–Enskog multiscale analysis, the reactive NS equations are recovered and the nonequilibrium effects are derived in Sec. III.

Section IV presents numerical tests, and Sec. V provides a summary and conclusions.

II. DISCRETE BOLTZMANN METHOD

In the Bhatnagar–Gross–Krook (BGK) model,^{43,44} a single relaxation time τ determines all discrete distribution functions approaching their equilibria at the same speed, and the Prandtl number is fixed at $Pr = 1$. To overcome this shortage, we construct an MRT DBM to make the Prandtl number adjustable, which takes the form

$$\frac{\partial \mathbf{f}}{\partial t} + \mathbf{V} \cdot \nabla \mathbf{f} = -\mathbf{S}(\hat{\mathbf{f}} - \hat{\mathbf{f}}^{eq}) + \mathbf{R} + \mathbf{F} + \mathbf{A}, \quad (1)$$

where $\mathbf{f} = (f_1, f_2, \dots, f_N)^\top$ and $\mathbf{f}^{eq} = (f_1^{eq}, f_2^{eq}, \dots, f_N^{eq})^\top$ stand for discrete distribution functions and their equilibrium counterparts in velocity space, respectively. $\hat{\mathbf{f}} = (\hat{f}_1, \hat{f}_2, \dots, \hat{f}_N)^\top$ and $\hat{\mathbf{f}}^{eq} = (\hat{f}_1^{eq}, \hat{f}_2^{eq}, \dots, \hat{f}_N^{eq})^\top$ denote kinetic moments of discrete distribution function and their equilibrium counterparts, respectively. Here, the subscript $N = 30$ is the total number of discrete velocities. In fact, the terms in moment space are transformed from those in velocity space by a transformation matrix \mathbf{M} , which is a square matrix with $N \times N$ elements in terms of discrete velocities. The elements of the transformation matrix are given in the Appendix. Specifically,

$$\hat{\mathbf{f}} = \mathbf{M}\mathbf{f}, \quad (2)$$

$$\hat{\mathbf{f}}^{eq} = \mathbf{M}\mathbf{f}^{eq}. \quad (3)$$

Similarly, $\mathbf{R} = (R_1, R_2, \dots, R_N)^\top$ and $\mathbf{F} = (F_1, F_2, \dots, F_N)^\top$ stand for the reaction and force terms in velocity space, respectively. $\hat{\mathbf{R}} = \mathbf{M}\mathbf{R}$ and $\hat{\mathbf{F}} = \mathbf{M}\mathbf{F}$ stand for discrete reaction and force terms in moment space, respectively. $\mathbf{S} = \text{diag}(S_1, S_2, \dots, S_N)^\top$ is a diagonal matrix that consists of relaxation coefficients S_i determining the speed of \hat{f}_i approaching \hat{f}_i^{eq} . The additional term $\hat{\mathbf{A}} = \mathbf{M}\mathbf{A} = (0, \dots, 0, \hat{A}_{12}, \hat{A}_{13}, \hat{A}_{14}, 0, \dots, 0)^\top$ is used to modify the collision operator so that the discrete Boltzmann equations could recover the correct reactive NS equations via the Chapman–Enskog analysis in terms of

$$\begin{aligned} \hat{A}_{12} = & \frac{S_{12} - S_6}{S_6} 4\rho T u_x \left[\frac{1}{D+I} \left(\frac{\partial u_x}{\partial x} + \frac{\partial u_y}{\partial y} + \frac{\partial u_z}{\partial z} \right) - \frac{\partial u_x}{\partial x} \right] \\ & + \frac{S_9 - S_{12}}{S_9} 2\rho T u_y \left(\frac{\partial u_y}{\partial x} + \frac{\partial u_x}{\partial y} \right) \\ & + \frac{S_{10} - S_{12}}{S_{10}} 2\rho T u_z \left(\frac{\partial u_z}{\partial x} + \frac{\partial u_x}{\partial z} \right), \end{aligned} \quad (4)$$

$$\begin{aligned} \hat{A}_{13} = & \frac{S_{13} - S_7}{S_7} 4\rho T u_y \left[\frac{1}{D+I} \left(\frac{\partial u_x}{\partial x} + \frac{\partial u_y}{\partial y} + \frac{\partial u_z}{\partial z} \right) - \frac{\partial u_y}{\partial y} \right] \\ & + \frac{S_9 - S_{13}}{S_9} 2\rho T u_x \left(\frac{\partial u_y}{\partial x} + \frac{\partial u_x}{\partial y} \right) \\ & + \frac{S_{11} - S_{13}}{S_{11}} 2\rho T u_z \left(\frac{\partial u_z}{\partial y} + \frac{\partial u_y}{\partial z} \right), \end{aligned} \quad (5)$$

$$\begin{aligned} \hat{A}_{14} = & \frac{S_{14} - S_8}{S_8} 4\rho T u_z \left[\frac{1}{D+I} \left(\frac{\partial u_x}{\partial x} + \frac{\partial u_y}{\partial y} + \frac{\partial u_z}{\partial z} \right) - \frac{\partial u_z}{\partial z} \right] \\ & + \frac{S_{10} - S_{14}}{S_{10}} 2\rho T u_x \left(\frac{\partial u_z}{\partial x} + \frac{\partial u_x}{\partial z} \right) \\ & + \frac{S_{11} - S_{14}}{S_{11}} 2\rho T u_y \left(\frac{\partial u_z}{\partial y} + \frac{\partial u_y}{\partial z} \right), \end{aligned} \quad (6)$$

where ρ , T , $p(= \rho T)$, and u_α are the density, temperature, pressure, and velocity, respectively. Here, $D = 3$ stands for the number of dimensions and I represents the extra degrees of freedom.

The discrete equilibrium distribution function satisfies the following moment relations:

$$\rho = \sum_i f_i^{eq} = \sum_i f_i, \quad (7)$$

$$\rho u_\alpha = \sum_i f_i^{eq} v_{i\alpha} = \sum_i f_i v_{i\alpha}, \quad (8)$$

$$\rho[(D+I)T + u^2] = \sum_i f_i^{eq} (v_i^2 + \eta_i^2) = \sum_i f_i (v_i^2 + \eta_i^2), \quad (9)$$

$$\rho(\delta_{\alpha\beta} T + u_\alpha u_\beta) = \sum_i f_i^{eq} v_{i\alpha} v_{i\beta}, \quad (10)$$

$$\rho u_\alpha [(D+I+2)T + u^2] = \sum_i f_i^{eq} (v_i^2 + \eta_i^2) v_{i\alpha}, \quad (11)$$

$$\rho(u_\alpha \delta_{\beta\chi} + u_\beta \delta_{\alpha\chi} + u_\chi \delta_{\alpha\beta}) T + \rho u_\alpha u_\beta u_\chi = \sum_i f_i^{eq} v_{i\alpha} v_{i\beta} v_{i\chi}, \quad (12)$$

$$\begin{aligned} \rho \delta_{\alpha\beta} [(D+I+2)T + u^2] T + \rho u_\alpha u_\beta [(D+I+4)T + u^2] \\ = \sum_i f_i^{eq} (v_i^2 + \eta_i^2) v_{i\alpha} v_{i\beta}. \end{aligned} \quad (13)$$

Here, α , β , and χ denote the direction that can be x , y , or z . Based on physical considerations and following the model proposed by Bourgat *et al.*,⁴⁵ we introduce a single additional variable I to represent non-translational degrees of freedom and utilize a free parameter η_i to describe molecular rotation and/or internal vibration energies. The specific heat ratio is defined as $\gamma = (D+I+2)/(D+I)$.

According to Eqs. (3) and (7)–(13), the discrete equilibrium distribution functions can be expressed as

$$\mathbf{f}^{eq} = \mathbf{M}^{-1} \hat{\mathbf{f}}^{eq}. \quad (14)$$

To ensure the matrix \mathbf{M} invertible and get better stability, we improve the discrete velocity model D3V30 proposed by Gan *et al.*⁴² Instead of using one parameter, we adopt four parameters v_a , v_b , v_c , and v_d to determine the magnitude of four sets of discrete velocities, respectively, in terms of

$$\mathbf{v}_i = \begin{cases} \mathbf{cyc} : v_a(\pm 1, 0, 0), & 1 \leq i \leq 6 \\ \mathbf{cyc} : v_b(\pm 1, \pm 1, 0), & 7 \leq i \leq 18 \\ \mathbf{cyc} : v_c(\pm 1, \pm 1, \pm 1), & 19 \leq i \leq 26 \\ v_d \cdot \mathbf{v}_i^{anti}, & 27 \leq i \leq 30, \end{cases} \quad (15)$$

with $\eta_i = \eta_0$ when i is an odd number; otherwise, $\eta_i = 0$. Here, **cyc** denotes a fully symmetric set of points. The antisymmetric part \mathbf{v}_i^{anti} ($27 \leq j \leq 30$) is proposed to guarantee the existence of \mathbf{M}^{-1} and, in this paper, is chosen as

$$\mathbf{v}_{27}^{anti} = \begin{bmatrix} -1 \\ 1 \\ 2 \end{bmatrix}, \mathbf{v}_{28}^{anti} = \begin{bmatrix} -2 \\ 2 \\ -2 \end{bmatrix}, \mathbf{v}_{29}^{anti} = \begin{bmatrix} 2 \\ -1 \\ -1 \end{bmatrix}, \mathbf{v}_{30}^{anti} = \begin{bmatrix} 1 \\ -2 \\ 1 \end{bmatrix}. \quad (16)$$

More forms of the antisymmetric part can be found in Ref. 42.

In Eqs. (7)–(9), we see f_i^{eq} can be replaced by f_i according to the conservation laws. However, in Eqs. (10)–(13), replacing f_i^{eq} with f_i may lead to the imbalance between left and right sides. The differences are actually departures of high order kinetic moments from their equilibria and can be utilized to investigate the nonequilibrium effects. We define the following nonequilibrium quantities:

$$\Delta_i = \hat{f}_i - \hat{f}_i^{eq} = \sum_j (f_j - f_j^{eq}) \mathbf{M}_{ij}. \quad (17)$$

Moreover, we introduce the symbols

$$\Delta_{v_\alpha v_\beta} = \sum_i (f_i - f_i^{eq}) v_{i\alpha} v_{i\beta}, \quad (18)$$

linked with the viscous stress tensor,

$$\Delta_{(v^2 + \eta^2) v_\alpha} = \sum_i (f_i - f_i^{eq}) (v_i^2 + \eta_i^2) v_{i\alpha}, \quad (19)$$

$$\Delta_{v_\alpha v_\beta v_\chi} = \sum_i (f_i - f_i^{eq}) v_{i\alpha} v_{i\beta} v_{i\chi}, \quad (20)$$

related to the nonorganized energy fluxes, and

$$\Delta_{(v^2 + \eta^2) v_\alpha v_\beta} = \sum_i (f_i - f_i^{eq}) (v_i^2 + \eta_i^2) v_{i\alpha} v_{i\beta}, \quad (21)$$

associated with the flux of nonorganized energy flux. Physically, $\frac{1}{2} \sum_i f_i v_{i\alpha}^2$ is defined as the translational energy in the α direction, and $\frac{1}{2} \sum_i f_i^{eq} v_{i\alpha}^2$ is its equilibrium counterpart. The nonequilibrium part $\frac{1}{2} \Delta_{v_\alpha v_\alpha}$ is the nonorganized energy in the α direction, which corresponds to the molecular individualism on top of the collective motion. Clearly, the DBM can provide the above nonequilibrium information beyond traditional NS equations.

The force and reaction terms are the variation rates of the distribution functions resulting from the external force and chemical reaction, respectively. The two terms are derived based on the following assumptions:

- (1) Over a small time interval, the change of the distribution function due to the external force and the chemical reaction can be treated as the change of the equilibrium distribution function, which is the leading part of the distribution function when the system is not too far from the equilibrium state.⁴⁶
- (2) The effect of the external force is to change the hydrodynamic velocity \mathbf{u} with the acceleration \mathbf{a} . In a small time interval, the velocity becomes $\mathbf{u}^\dagger = \mathbf{u} + \mathbf{a}\tau$.
- (3) The temporal scale of the chemical reaction is much smaller than that of fluid flow, and the chemical reaction leads to the

change of energy with the varying rate,

$$E' = \rho Q \lambda', \quad (22)$$

where Q indicates the chemical heat release per unit mass of fuel and λ indicates the mass fraction of chemical product. From Eq. (9), we obtain the temperature after the chemical reaction $T^\diamond = T + \tau T'$ with the varying rate of temperature $T' = 2Q\lambda'/(D + I)$.

Now, we can derive the force term,

$$F_i = \frac{1}{\tau} [f_i^{eq}(\rho, \mathbf{u}^\dagger, T) - f_i^{eq}(\rho, \mathbf{u}, T)], \quad (23)$$

and the reaction term,

$$R_i = \frac{1}{\tau} [f_i^{eq}(\rho, \mathbf{u}, T^\diamond) - f_i^{eq}(\rho, \mathbf{u}, T)]. \quad (24)$$

The discrete forms F_i and R_i satisfy the relation

$$\iint F \Psi d\mathbf{v} d\eta = \sum_i F_i \Psi_i, \quad (25)$$

$$\iint R \Psi d\mathbf{v} d\eta = \sum_i R_i \Psi_i, \quad (26)$$

with $\Psi = 1, \mathbf{v}_i, (\mathbf{v}_i \cdot \mathbf{v}_i + \eta_i^2), \mathbf{v}_i \mathbf{v}_i, (\mathbf{v}_i \cdot \mathbf{v}_i + \eta_i^2) \mathbf{v}_i, \mathbf{v}_i \mathbf{v}_i \mathbf{v}_i$ and $(\mathbf{v}_i \cdot \mathbf{v}_i + \eta_i^2) \mathbf{v}_i \mathbf{v}_i$, respectively. Substituting Eqs. (7)–(13) into Eqs. (23) and (24) results in $\hat{\mathbf{F}} = \mathbf{M}\mathbf{F}$ and $\hat{\mathbf{R}} = \mathbf{M}\mathbf{R}$, respectively, and the elements of the force and reaction terms are given in the Appendix.

To describe the dynamics of detonations and compare with the previous study on the instability of detonations, we consider a simple model of a chemical reaction between two perfect gases, assuming irreversible, one-step Arrhenius kinetics,

$$\lambda' = K(1 - \lambda) \exp\left(-\frac{E_a}{T}\right), \quad (27)$$

where K is the rate constant and E_a is the activation energy.

The DBM employs larger velocity stencil and introduces higher-order moments, by which the hydrodynamic and thermodynamic fields are fully coupled. It is also worth mentioning that we utilize the matrix inversion method here instead of the commonly adopted polynomial approach where equilibrium distribution functions are expanded upon the terms of the macroscopic quantities due to the following merits. The number of discrete velocities of the DBM equals exactly the number of required kinetic moments of equilibrium discrete distribution functions, while the polynomial method always requires more discrete velocities because the discrete velocity sets of the latter should have enough isotropy to recover the hydrodynamic equations correctly.^{47,48} Consequently, the presented method is more efficient. Additionally, in the DBM, each kinetic moment computed by summation of the discrete equilibrium distribution functions is exactly equal to the one calculated by integral of the Maxwellian function. Furthermore, the discrete Boltzmann equations are expressed in a uniform form, and thus, the DBM is easier to code. The DBM code is parallelized on the UK National Supercomputing Service ARCHER and runs efficiently.

III. THE CHAPMAN-ENSKOG ANALYSIS

In this section, we show the main procedure of the Chapman–Enskog analysis. With respect to an expansion parameter ε , which is a quantity of the order of the Knudsen number,⁴⁹ we introduce the following expansions:

$$f_i = f_i^{(0)} + f_i^{(1)} + f_i^{(2)} + \dots, \tag{28}$$

$$\frac{\partial}{\partial t} = \frac{\partial}{\partial t_1} + \frac{\partial}{\partial t_2} + \dots, \tag{29}$$

$$\frac{\partial}{\partial r_\alpha} = \frac{\partial}{\partial r_{1\alpha}}, \tag{30}$$

$$A_i = A_{1i}, \tag{31}$$

$$F_i = F_{1i}, \tag{32}$$

$$R_i = R_{1i}, \tag{33}$$

where the part of distribution function $f_i^{(k)} = O(\varepsilon^k)$, the temporal derivative $\frac{\partial}{\partial t_k} = O(\varepsilon^k)$, the spatial derivative $\frac{\partial}{\partial r_{1\alpha}} = O(\varepsilon)$, $A_{1i} = O(\varepsilon)$, $F_{1i} = O(\varepsilon)$, and $R_{1i} = O(\varepsilon)$ ($k = 1, 2, \dots$). By substituting Eqs. (28)–(33) into Eq. (1), we can obtain the following equations in consecutive order of the parameter ε :

$$O(\varepsilon^0) : \dot{\mathbf{f}}^{(0)} = \hat{\mathbf{f}}^{eq}, \tag{34}$$

$$O(\varepsilon^1) : \left(\frac{\partial}{\partial t_1} + \hat{\mathbf{E}} \cdot \nabla_1 \right) \dot{\mathbf{f}}^{(0)} = -\mathbf{S}\dot{\mathbf{f}}^{(1)} + \hat{\mathbf{A}} + \hat{\mathbf{F}} + \hat{\mathbf{R}}, \tag{35}$$

$$O(\varepsilon^2) : \frac{\partial}{\partial t_2} \dot{\mathbf{f}}^{(0)} + \left(\frac{\partial}{\partial t_1} + \hat{\mathbf{E}} \cdot \nabla_1 \right) \dot{\mathbf{f}}^{(1)} = -\mathbf{S}\dot{\mathbf{f}}^{(2)}, \tag{36}$$

with $\hat{\mathbf{E}} = \mathbf{M}\mathbf{V}\mathbf{M}^{-1}$. Equations (34)–(36) are expressed by the vector equality and consist of N scalar relations. Substituting the moments of Eqs. (7)–(11) into the first five relations of Eq. (35), we can obtain the following macroscopic equations on the $t_1 = \varepsilon t$ time scale and $\mathbf{r}_1 = \varepsilon \mathbf{r}$ space scale:

$$\frac{\partial \rho}{\partial t_1} + \rho \frac{\partial u_\alpha}{\partial r_\alpha} + u_\alpha \frac{\partial \rho}{\partial r_\alpha} = 0, \tag{37}$$

$$\frac{\partial j_\alpha}{\partial t_1} + \frac{\partial \rho (\delta_{\alpha\beta} T + u_\alpha u_\beta)}{\partial r_\alpha} = \rho a_\alpha, \tag{38}$$

$$\frac{\partial \xi}{\partial t_1} + \frac{\partial \rho u_\alpha [(D+I+2)T + u^2]}{\partial r_\alpha} = 2\rho u_\alpha a_\alpha + 2\rho \lambda' Q, \tag{39}$$

where $j_\alpha = \rho u_\alpha$ is the momentum and $\xi = (D+I)\rho T + (j_x^2 + j_y^2 + j_z^2)/\rho$ is twice the total energy. Combining Eqs. (37)–(39)

and the sixth to the fourteenth relations of Eq. (35), we can derive the following quantities:

$$S_6 \hat{f}_6^{(1)} = -2\rho T \frac{\partial u_x}{\partial x} + \frac{2\rho T}{D+I} \left(\frac{\partial u_x}{\partial x} + \frac{\partial u_y}{\partial y} + \frac{\partial u_z}{\partial z} \right), \tag{40}$$

$$S_7 \hat{f}_7^{(1)} = -2\rho T \frac{\partial u_y}{\partial y} + \frac{2\rho T}{D+I} \left(\frac{\partial u_x}{\partial x} + \frac{\partial u_y}{\partial y} + \frac{\partial u_z}{\partial z} \right), \tag{41}$$

$$S_8 \hat{f}_8^{(1)} = -2\rho T \frac{\partial u_z}{\partial z} + \frac{2\rho T}{D+I} \left(\frac{\partial u_x}{\partial x} + \frac{\partial u_y}{\partial y} + \frac{\partial u_z}{\partial z} \right), \tag{42}$$

$$S_9 \hat{f}_9^{(1)} = -\rho T \frac{\partial u_x}{\partial y} - \rho T \frac{\partial u_y}{\partial x}, \tag{43}$$

$$S_{10} \hat{f}_{10}^{(1)} = -\rho T \frac{\partial u_x}{\partial z} - \rho T \frac{\partial u_z}{\partial x}, \tag{44}$$

$$S_{11} \hat{f}_{11}^{(1)} = -\rho T \frac{\partial u_z}{\partial y} - \rho T \frac{\partial u_y}{\partial z}, \tag{45}$$

$$S_{12} \hat{f}_{12}^{(1)} = \rho T \left[\frac{4u_x}{D+I} \left(\frac{\partial u_x}{\partial x} + \frac{\partial u_y}{\partial y} + \frac{\partial u_z}{\partial z} \right) - 4u_x \frac{\partial u_x}{\partial x} - 2u_y \left(\frac{\partial u_x}{\partial y} + \frac{\partial u_y}{\partial x} \right) - 2u_z \left(\frac{\partial u_x}{\partial z} + \frac{\partial u_z}{\partial x} \right) - (D+I+2) \frac{\partial T}{\partial x} \right] + \hat{A}_{12}, \tag{46}$$

$$S_{13} \hat{f}_{13}^{(1)} = \rho T \left[\frac{4u_y}{D+I} \left(\frac{\partial u_x}{\partial x} + \frac{\partial u_y}{\partial y} + \frac{\partial u_z}{\partial z} \right) - 4u_y \frac{\partial u_y}{\partial y} - 2u_x \left(\frac{\partial u_x}{\partial y} + \frac{\partial u_y}{\partial x} \right) - 2u_z \left(\frac{\partial u_y}{\partial z} + \frac{\partial u_z}{\partial y} \right) - (D+I+2) \frac{\partial T}{\partial y} \right] + \hat{A}_{13}, \tag{47}$$

$$S_{14} \hat{f}_{14}^{(1)} = \rho T \left[\frac{4u_z}{D+I} \left(\frac{\partial u_x}{\partial x} + \frac{\partial u_y}{\partial y} + \frac{\partial u_z}{\partial z} \right) - 4u_z \frac{\partial u_z}{\partial z} - 2u_x \left(\frac{\partial u_x}{\partial z} + \frac{\partial u_z}{\partial x} \right) - 2u_y \left(\frac{\partial u_y}{\partial z} + \frac{\partial u_z}{\partial y} \right) - (D+I+2) \frac{\partial T}{\partial z} \right] + \hat{A}_{14}. \tag{48}$$

The additional terms in Eqs. (46)–(48) are determined in Eqs. (4)–(6), which are used to modify the collision terms so that the NS equations can be correctly recovered. In the case that the system is isothermal, the additional terms can be eliminated.

The above quantities \hat{f}_i are the exact solutions of nonequilibrium quantities on the level of the first order accuracy. Similar to the

above derivation of $t_1 = \epsilon t$ scale, the macroscopic equations on the $t_2 = \epsilon^2 t$ time scale are derived by the first five relations in Eq. (36),

$$\frac{\partial \rho}{\partial t_2} = 0, \tag{49}$$

$$\frac{\partial j_x}{\partial t_2} + \frac{\partial \hat{f}_6^{(1)}}{\partial x_1} + \frac{\partial \hat{f}_9^{(1)}}{\partial y_1} + \frac{\partial \hat{f}_{10}^{(1)}}{\partial z_1} = 0, \tag{50}$$

$$\frac{\partial j_y}{\partial t_2} + \frac{\partial \hat{f}_9^{(1)}}{\partial x_1} + \frac{\partial \hat{f}_7^{(1)}}{\partial y_1} + \frac{\partial \hat{f}_{11}^{(1)}}{\partial z_1} = 0, \tag{51}$$

$$\frac{\partial j_z}{\partial t_2} + \frac{\partial \hat{f}_{10}^{(1)}}{\partial x_1} + \frac{\partial \hat{f}_{11}^{(1)}}{\partial y_1} + \frac{\partial \hat{f}_8^{(1)}}{\partial z_1} = 0, \tag{52}$$

$$\frac{\partial \xi}{\partial t_2} + \frac{\partial \hat{f}_{12}^{(1)}}{\partial x_1} + \frac{\partial \hat{f}_{13}^{(1)}}{\partial y_1} + \frac{\partial \hat{f}_{14}^{(1)}}{\partial z_1} = 0. \tag{53}$$

With the aid of Eqs. (37)–(48), the final equations can be written as

$$\frac{\partial \rho}{\partial t} + \frac{\partial j_\alpha}{\partial r_\alpha} = 0, \tag{54}$$

$$\frac{\partial j_\alpha}{\partial t} + \frac{\partial p}{\partial r_\alpha} + \frac{\partial}{\partial r_\beta} (\rho u_\alpha u_\beta + P_{\alpha\beta}) = \rho a_\alpha, \tag{55}$$

$$\begin{aligned} \frac{\partial \xi}{\partial t} + \frac{\partial (\xi + 2p) u_\alpha}{\partial r_\alpha} - 2 \frac{\partial}{\partial r_\beta} \left(\kappa_\beta \frac{\partial T}{\partial r_\beta} - P_{\alpha\beta} u_\alpha \right) \\ = 2\rho u_\alpha a_\alpha + 2\rho \lambda' Q \end{aligned} \tag{56}$$

in terms of

$$P_{\alpha\beta} = \frac{\rho T}{S_{\alpha\beta}} \left(\frac{2\delta_{\alpha\beta}}{D+I} \frac{\partial u_\chi}{\partial r_\chi} - \frac{\partial u_\alpha}{\partial r_\beta} - \frac{\partial u_\beta}{\partial r_\alpha} \right), \tag{57}$$

where $S_{xx} = S_6$, $S_{yy} = S_7$, $S_{zz} = S_8$, $S_{xy} = S_9$, $S_{xz} = S_{10}$, and $S_{yz} = S_{11}$.

Here, we explain the reason for the additional term. Mathematically, we can adjust the relaxation coefficients independently. From the point view of physics, the coefficients are not completely independent for the system with isotropy constraints.⁵⁰ From the derivation, we can see that S_1 , S_2 , S_3 , S_4 , and S_5 have no influence on the equation due to the conservation laws. However, in order to recover the NS equations in the continuity limit, the terms referring to the stress tensor and the energy flux should be coupled, respectively, which leads to

$$S_6 = S_7 = S_8 = S_9 = S_{10} = S_{11} = S_\mu, \tag{58}$$

related to viscosity, and

$$S_{12} = S_{13} = S_{14} = \hat{S}_\kappa, \tag{59}$$

related to heat conductivity, and then Eqs. (54)–(56) reduce to

$$\frac{\partial \rho}{\partial t} + \frac{\partial j_\alpha}{\partial r_\alpha} = 0, \tag{60}$$

$$\frac{\partial j_\alpha}{\partial t} + \frac{\partial p}{\partial r_\alpha} + \frac{\partial}{\partial r_\beta} (\rho u_\alpha u_\beta + P_{\alpha\beta}) = \rho a_\alpha, \tag{61}$$

$$\begin{aligned} \frac{\partial \xi}{\partial t} + \frac{\partial (\xi + 2p) u_\alpha}{\partial r_\alpha} - 2 \frac{\partial}{\partial r_\beta} \left(\kappa \frac{\partial T}{\partial r_\beta} - P_{\alpha\beta} u_\alpha \right) \\ = 2\rho u_\alpha a_\alpha + 2\rho \lambda' Q, \end{aligned} \tag{62}$$

where

$$P_{\alpha\beta} = -\mu \left(\frac{\partial u_\alpha}{\partial r_\beta} + \frac{\partial u_\beta}{\partial r_\alpha} - \frac{2}{D} \frac{\partial u_\chi}{\partial r_\chi} \delta_{\alpha\beta} \right) - \mu_B \frac{\partial u_\chi}{\partial r_\chi} \delta_{\alpha\beta}, \tag{63}$$

and the dynamic viscosity μ , the bulk viscosity μ_B , and the thermal conductivity κ are defined as

$$\mu = \frac{\rho T}{S_\mu}, \tag{64}$$

$$\mu_B = \mu \left(\frac{2}{D} - \frac{2}{D+I} \right), \tag{65}$$

and

$$\kappa = \left(\frac{D+I}{2} + 1 \right) \frac{\rho T}{S_\kappa}, \tag{66}$$

respectively. Furthermore, the Prandtl number,

$$\text{Pr} = \frac{c_p \mu}{\kappa} = \frac{S_\kappa}{S_\mu}, \tag{67}$$

is adjustable in the model. In conclusion, we modify the collision operator by the additional term so that the NS equations can be recovered correctly. Specifically, we can find that the nonequilibrium quantity

$$\Delta_{v_\alpha v_\beta} = P_{\alpha\beta} \tag{68}$$

is just the viscous stress tensor, and

$$\Delta_{(v^2 + \eta^2) v_\alpha} = -\kappa \frac{\partial T}{\partial r_\beta} + P_{\alpha\beta} u_\alpha \tag{69}$$

is related to the thermal conductivity (see Ref. 51). As we can see, the diagonal matrix \mathbf{S} controls the speed of f_i approaching its equilibrium counterpart \hat{f}_i^{eq} and the elements of the matrix S_i are related to the thermodynamic nonequilibrium manifestations. S_1 , S_2 – S_4 , and S_5 are related to mass, momentum, and energy conservation, respectively. Actually, the values of the above coefficients have no effect on the flow system due to the conservation laws. S_6 – S_{11} are related to dynamic viscosity and S_{12} – S_{14} are linked with heat conductivity in the NS equations. Finally, S_{15} – S_{24} are associated with nonorganized energy fluxes and S_{25} – S_{30} correspond to the flux of nonorganized energy flux.

IV. NUMERICAL TESTS

To validate the proposed model and showcase its performance, we show simulation results of some classical benchmarks. First, we simulate the free falling process with a chemical reaction to

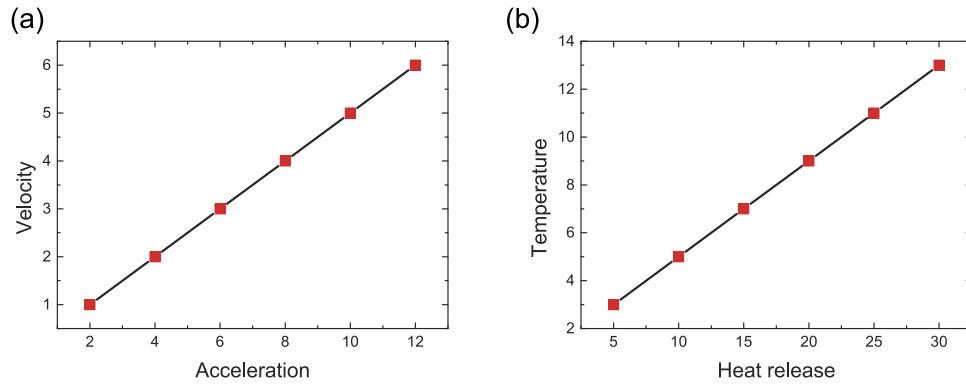


FIG. 1. Free falling process in a box with chemical reaction and external force. (a) Velocity vs acceleration; and (b) temperature vs heat release. The symbols denote the DBM results, and the lines represent the theoretical solutions.

investigate the model in the flow field coupled with a chemical reaction and external force. Then, we simulate the thermal Couette flow to verify that both the specific heat ratio and Prandtl number are adjustable. Furthermore, we simulate a 1D detonation to show that the model is capable of describing supersonic flows and measuring the nonequilibrium effects. Finally, a spherical explosion is modeled to demonstrate the ability of the proposed model to deal with a 3D configuration. In this work, we utilize the third-order Runge–Kutta scheme for the time derivative in Eq. (1) and the second-order nonoscillatory and nonfree-parameter dissipation difference scheme for the space derivative.⁵²

A. Chemical reaction in the free falling process

The exothermic chemical reaction in a free falling box is simulated as the first numerical test. At the beginning, the box is filled with the chemical reactant and the initial physical quantities are density $\rho_0 = 1$, velocity $\mathbf{u}_0 = 0$, and temperature $T_0 = 1.0$. Since the field is uniform, we use only one mesh to simulate the process, and thus, the computational domain is $N_x \times N_y \times N_z = 1 \times 1 \times 1$, where the periodic boundary is used in each direction. We choose Δx

$= \Delta y = \Delta z = 10^{-3}$ as the spatial step and $\Delta t = 10^{-4}$ as the temporal step. Reaction parameters are $K = 5 \times 10^2$ and $E_a = 8$, and relaxation coefficients are $S_i = 10^4$.

Figure 1(a) plots the vertical velocity u_z vs various acceleration $\mathbf{a} = a_z \mathbf{e}_z$ with fixed chemical reaction heat release $Q = 10$ at time $t = 0.5$. The theoretical vertical velocity in the external force field is $u_z = a_z t$. Figure 1(b) illustrates the temperature T vs chemical heat release with fixed acceleration $a_z = 10$. The theoretical solution for temperature after the chemical reaction is $T = T_0 + (\gamma - 1)Q$. From the above pictures, we can find the simulation results match well with the analytical ones, which shows good performance of the model to describe the effects of the external force and chemical reaction.

B. Thermal Couette flow

To validate that the model can be used with the adjustable specific heat ratio and Prandtl number, the thermal Couette flow is simulated here. The initial configuration is a viscous fluid flow between two infinite parallel flat plates, and the physical quantity of the flow is $\rho_0 = 1$, $\mathbf{u}_0 = 0$, and $T_0 = 1$. The plate below the flow is

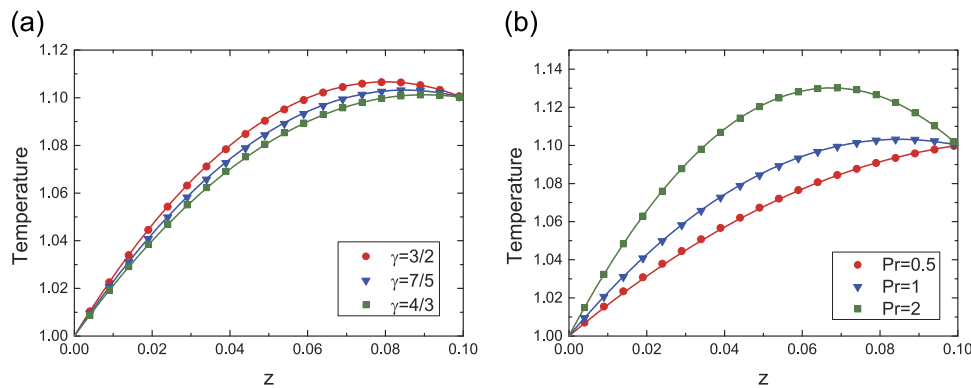


FIG. 2. Temperature profiles of thermal Couette flow. (a) Temperature distribution for cases with various specific heat ratios. (b) Temperature distribution for cases with various Prandtl numbers. Symbols denote the results of the DBM, and solid lines represent the exact solutions.

stationary with temperature $T_L = 1$, and the top plate moves along the horizontal direction with a constant speed $u_x = 1$ and temperature $T_U = 1.1$. The distance between the plates is $H = 0.1$. We carry out the simulation with $\Delta x = \Delta y = \Delta z = 10^{-3}$, $\Delta t = 10^{-4}$, $\nu_a = \nu_b = \nu_c = \nu_d = 1.6$, and $\eta_0 = 2.1$, and the grid mesh is $N_x = N_y = N_z = 1 \times 1 \times 100$. Periodic boundary conditions are utilized in the x and y directions, and the nonequilibrium extrapolation method is applied in the z direction. The analytical solution to the temperature profile along the z direction is

$$T = T_L + (T_U - T_L) \frac{z}{H} + \frac{\mu}{2\kappa} u_x^2 \frac{z}{H} \left(1 - \frac{z}{H}\right). \quad (70)$$

Figure 2(a) shows the comparisons of the DBM simulation results and exact solutions of the temperature along the z direction with different specific heat ratios $\gamma = 3/2, 7/5$, and $4/3$ and fixed Prandtl number $Pr = 1.0$, where collision parameters $S_i = 2 \times 10^3$. It is evident that the simulation results agree excellently well with the analytical ones. Figure 2(b) plots the temperature distribution with various Prandtl numbers $Pr = 0.5, 1.0$, and 2.0 , where collision parameters $S_i = 2 \times 10^3$ and $S_\mu = 4 \times 10^3, 2 \times 10^3$, and 1×10^3 , respectively. The specific heat ratio is $7/5$ for the three cases. The simulation results also match well with the exact solutions for various Prandtl numbers.

C. One-dimensional detonation

In order to make the calculation simple and explicit, all the quantities have been made dimensionless by reference to the unburned state ahead of the detonation front. The reference length scale x_{ref} is chosen such that the half of 1D Zel'dovich, von Neumann, and Döring (ZND) induction length is unity,

$$\begin{aligned} \rho &= \frac{\tilde{\rho}}{\tilde{\rho}_0}, \\ p &= \frac{\tilde{p}}{\tilde{p}_0}, \\ T &= \frac{\tilde{T}}{\tilde{T}_0} = \tilde{T} \sqrt{\frac{\tilde{\rho}_0}{\tilde{p}_0}}, \\ u &= \frac{\tilde{u}}{c_0} = \frac{\tilde{u}}{\sqrt{\gamma \tilde{T}_0}}. \end{aligned} \quad (71)$$

Adopting the notations in Ref. 53, the symbol \sim stands for dimensional quantities and subscript 0 denotes the unburnt state.

Previous research indicates that the overdrive factor f (the square of the ratio of imposed detonation front velocity to the Chapman–Jouguet velocity), the specific heat ratio γ , the heat release Q , and the activation energy E_a are all related to the stability of the detonations.^{54–57}

In this part, we first simulate an unstable 1D detonation with the following parameters to verify the effectiveness of the model: $f = 1.6, \gamma = 1.2, Q = 50$, and $E_a = 50$. Given the above dimensionless values, the pre-exponential parameter equals $K = 230.75$. The initial condition is given by the theory developed independently by ZND. The physical domain is set to be $0 \leq x \leq 800$ with an inflow at the left boundary and an outflow at the right boundary. The periodic boundary condition is imposed on the upper and lower boundaries. The initial location of the ZND detonation front is set at $x = 8$.

We carry out the simulation with $\nu_a = 1.0, \nu_b = \nu_c = 4.5, \nu_d = 0.1, \eta_0 = 2.7$, and $S_i = 5 \times 10^3$. Different grid resolution δ_n (denotes the number of grid points per half-reaction length) is employed to find an appropriate resolution for computation effectiveness.

As common practice, we use the peak pressure, which is the maximum pressure at the precursor explosion, to validate the performance of the numerical schemes.^{54,56–58} Figure 3 shows temporal histories of the peak pressure under different resolutions. As one can see, all the results oscillate periodically for $t > 20$. The solution with the lower resolution δ_{50} yields a poor result. With the increase in the resolution, the higher resolutions δ_{75} and δ_{100} behave similarly. To further validate the accuracy of the DBM, we compare the maximum, minimum, and the period of the oscillations of the DBM $(P_{max}, P_{min}, T_{period}) = (99.05, 57.5, 7.25)$ with the predicted peak pressure ($P_{max} = 98.6$) in the literature⁵⁴ and the results $(P_{min}, T_{period}) = (57, 7.25)$ in Ref. 58. The data show that the DBM captures the detonation phenomenon well and both the amplitude and period agree well with the reference solutions in Refs. 54 and 58. Figure 4 illustrates profiles of the detonation wave: (a) pressure and (b) temperature at time $t = 77$ with resolutions δ_{75} and δ_{100} . Obviously, the results are, in general, in good agreement with Fig. 4.4 in Ref. 57.

In addition to the unstable detonation, we simulate a stable detonation with the following parameters: $f = 1.0, \gamma = 1.4, Q = 1.0$, and $E_a = 8.0$. The pre-exponential parameter equals $K = 122.77$. The physical domain is set to be $0 \leq x \leq 500$, and the initial location of the ZND detonation front is set at $x = 5$. For stable detonations, δ_{100} is used. The parameters adopted are $\nu_a = \nu_b = \nu_c = \nu_d = 1.8, \eta_0 = 2.0$, and $S_i = 2 \times 10^2$.

Figure 5 illustrates profiles of the detonation wave at time $t = 160$. The symbols stand for the DBM results, and the solid lines represent the ZND solutions. The numerical results behind the detonation are $(\rho, p, T, u_x) = (1.3895, 2.1930, 1.5829, 0.5781)$. Compared with the ZND solutions $(\rho, p, T, u_x) = (1.3884, 2.1966, 1.5786, 0.5774)$, the relative errors are $(0.079\%, 0.16\%, 0.27\%, 0.12\%)$,

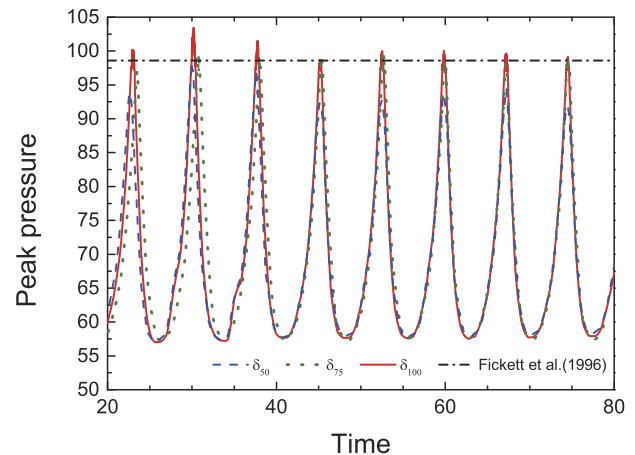


FIG. 3. Temporal histories of the peak pressure in the unstable detonation under different resolutions. The dashed, dotted, and solid lines denote the resolution δ_{50}, δ_{75} , and δ_{100} , respectively. The dashed-dotted line stands for the predicted peak pressure in Ref. 54.

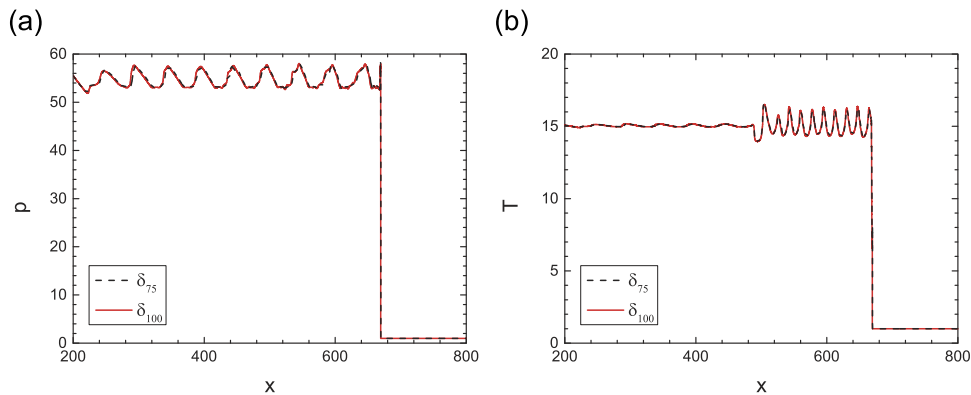


FIG. 4. Spatial profiles of (a) pressure and (b) temperature in the unstable detonation at time $t = 77$. Dashed lines denote the resolution δ_{75} , and solid lines stand for δ_{100} .

respectively. The results of the DBM have a satisfying coincidence with the ZND theory.

Figure 6 displays the kinetic moments and nonequilibrium quantity around the detonation wave at time $t = 160$ in order to demonstrate the capability of the DBM of capturing the nonequilibrium effects. Figures 6(a) and 6(b) illustrate the kinetic moment $\hat{f}_6 = \sum_i f_i v_{ix}^2$ and the equilibrium counterpart $\hat{f}_6^{eq} = \sum_i f_i^{eq} v_{ix}^2$ within $412 \leq x \leq 428$ and a more detailed domain where $424.4 \leq x \leq 424.7$,

respectively. The kinetic moment is the nonorganized energy in the x direction and the exact solution of the equilibrium kinetic moment is $\hat{f}_6^{eq} = \rho(T + u_x^2)$ [see Eq. (10)]. The squares and triangles denote \hat{f}_6 and \hat{f}_6^{eq} , respectively. The solid line represents the exact solution. As we can see, the nonorganized energy reaches the maximum at the front shock. The difference between the kinetic moment and the equilibrium counterpart is just the nonequilibrium quantity $\Delta_{xx} = \hat{f}_6 - \hat{f}_6^{eq}$ and is demonstrated in Figs. 6(c) and 6(d). In addition, the

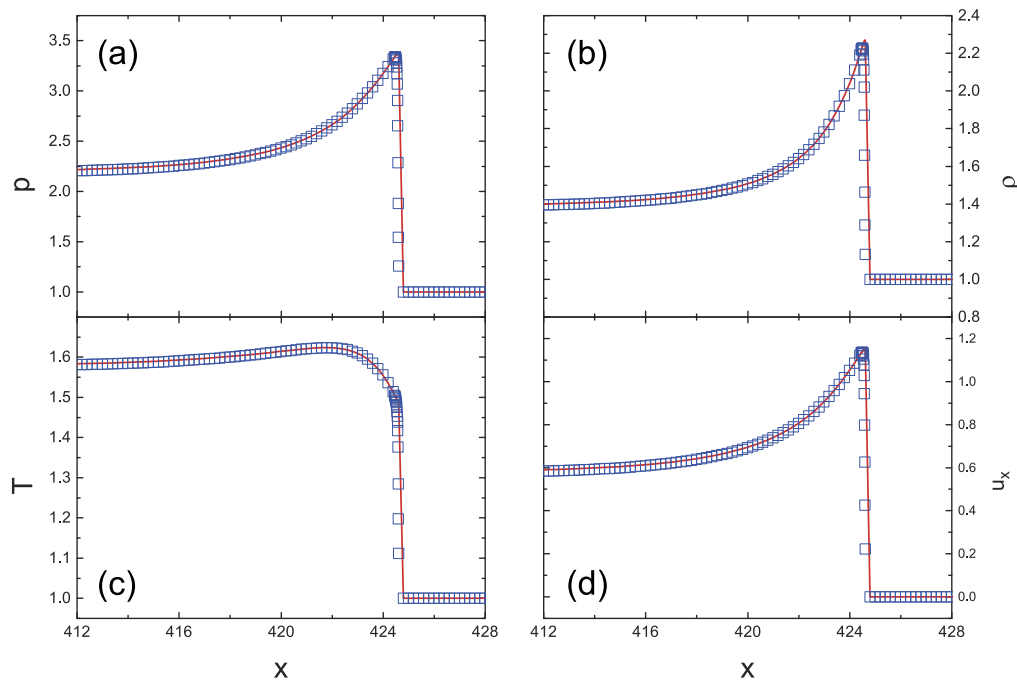


FIG. 5. Physical quantities of the stable detonation: (a) pressure, (b) density, (c) temperature, and (d) horizontal velocity. The symbols represent the DBM results, and the solid lines represent ZND solutions.

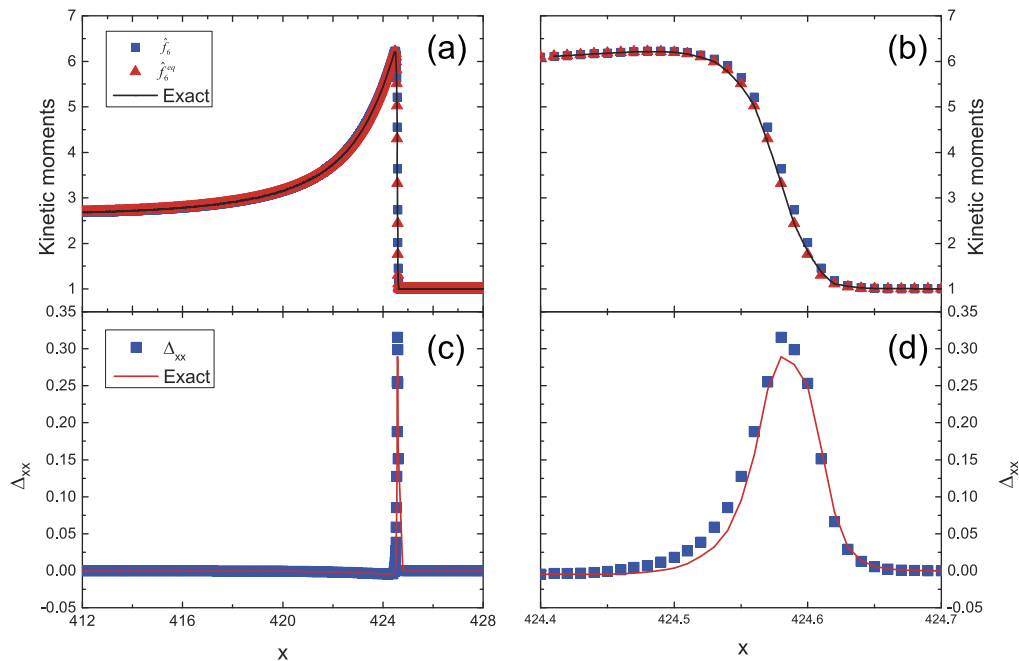


FIG. 6. Kinetic moments and nonequilibrium quantity around the detonation wave. (a) Kinetic moments within $412 \leq x \leq 428$, (b) kinetic moments around the front shock within $424.4 \leq x \leq 424.7$, (c) nonequilibrium quantity Δ_{xx} within $412 \leq x \leq 428$, and (d) nonequilibrium quantity Δ_{xx} around the front shock within $424.4 \leq x \leq 424.7$.

corresponding analytical solution by Eq. (40) is illustrated. The symbols stand for the solutions of the DBM, and the solid line represents the analytical solution. Obviously, the results of DBM are, in general, in good agreement with the analytical solutions. It can be found that there exist nonequilibrium effects in the reaction zone. In particular, around the front shock, the nonequilibrium effects are obvious. This result is physically reasonable. At the front shock, the chemical energy is continuously released and due to the rapid change of physical quantities, the system departs from its thermodynamic equilibrium state.

D. Three-dimensional explosion

In this part, we consider a 3D spherical explosion in a box with parameters: $\gamma = 1.2$, $Q = 2.0$, and $E_a = 1.0$. At the initial time, the system is at rest and the density and temperature are given as follows: $(\rho, T) = (2, 2)$ for $\sqrt{(i_x - 0.5N_x)^2 + (i_y - 0.5N_y)^2 + (i_z - 0.5N_z)^2} \leq 0.1N_x$ and others $(\rho, T) = (1, 1)$ with periodic boundary conditions at the surfaces. This configuration is symmetrical and can be utilized to verify the model by checking whether the mass and energy are conserved. We carry out the simulation with $\Delta x = \Delta y = \Delta z = 10^{-4}$, $\Delta t = 10^{-6}$, $v_a = v_b = v_c = v_d = 1.6$, $\eta_0 = 3.5$, and $S_i = 10^5$, and the grid mesh is $N_x \times N_y \times N_z = 200 \times 200 \times 200$.

To demonstrate the evolution process of the spherical explosion, we choose several typical snapshots of the pressure isosurfaces at various times in Fig. 7. Since the computational system is symmetrical, only half of the system is depicted for clear illustration. Figure 7(a) shows the initial configuration, and (b) and (c) display the evolution process at time $t = 0.0025$ and 0.005 , respectively. First,

the spherical shock wave expands in the enclosed box and contacts with the wall when $t = 0.005$. Afterward, the shock wave is reflected and propagates inwards with the increase in time. As we can see, the shocks are well captured in the DBM.

Figure 8 illustrates the temporal histories of the mass and energies in the explosion process. The total reactant mass decreases and the total product mass increases gradually due to the chemical reaction in the initial stage ($0 \leq t \leq 0.01154$). After the chemical reaction ends ($t > 0.01154$), the reactant density equals zero. The total mass remains constant in the whole evolution. Figure 8(b) shows in the evolution, the chemical energy decreases gradually and is transformed into the internal and kinetic energies, while the sum of all

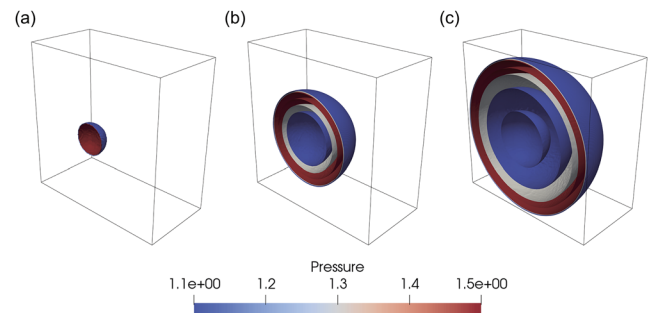


FIG. 7. Snapshots of the pressure isosurfaces in the spherical explosion process: (a) $t = 0$, (b) $t = 0.0025$, and (c) $t = 0.005$.

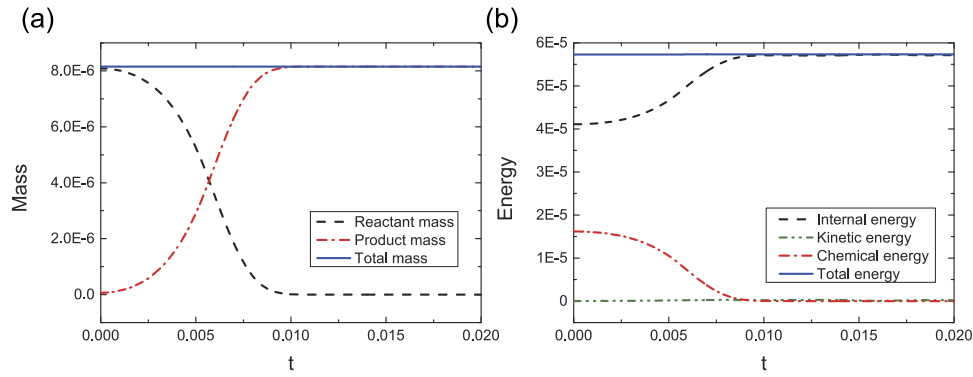


FIG. 8. The temporal histories of physical quantities. (a) Density; (b) internal, kinetic, chemical, and total energies.

energies remains unchanged. Figure 8 indicates that the mass and energy of the system are conserved. It is shown that the proposed DBM has a satisfying performance for simulations of 3D reacting flows.

V. CONCLUSION

In this paper, a 3D MRT DBM is presented for reactive flows where both the Prandtl number and specific heat ratio are freely adjustable. There are 30 kinetic moments of discrete distribution functions, and an efficient discrete velocity model, D3V30, is utilized. The NS equations can be recovered at macroscales from the DBM through the Chapman–Enskog analysis. Unlike existing LBMs for reactive flows, the hydrodynamic and thermodynamic fields are fully coupled in the DBM to simulate combustion in subsonic, supersonic, and potentially hypersonic flows. In addition, the nonequilibrium effects of the system can be probed and quantified. In this model, the reaction and force terms added into the discrete Boltzmann equation describe the change rates of discrete functions due to the chemical heat release and external force, respectively.

The DBM has been validated for several typical applications. The capability of the DBM to simulate the flow field fully coupled with a chemical reaction and external force is verified using the free falling reacting box. The case of the thermal Couette flow demonstrates that both the specific heat ratio and Prandtl number are adjustable. Furthermore, the DBM is shown to accurately simulate supersonic flows and quantify the nonequilibrium effects in 1D detonation. Finally, the main features of a spherical explosion in an enclosed box are successfully captured to showcase the ability of the DBM to deal with a 3D configuration. In conclusion, a new 3D DBM for reactive flows featuring full coupling of flow and combustion fields has been developed and successfully validated. This opens up possibilities for exploring a variety of reactive flows at subsonic, supersonic, and hypersonic speeds with both hydrodynamic and thermodynamic nonequilibria.

ACKNOWLEDGMENTS

This work was supported by the National Natural Science Foundation of China (NSFC) under Grant No. 51806116 and the Center for Combustion Energy at Tsinghua University. Support

from the UK Engineering and Physical Sciences Research Council under the project UK Consortium on Mesoscale Engineering Sciences (UKCOMES) (Grant No. EP/R029598/1) is also gratefully acknowledged.

APPENDIX: TRANSFORMATION MATRIX AND KINETIC MOMENTS

The equilibrium distribution function is

$$f^{eq} = \rho \left(\frac{m}{2\pi T} \right)^{D/2} \left(\frac{m}{2\pi IT} \right)^{1/2} \exp \left[-\frac{m|\mathbf{v} - \mathbf{u}|^2}{2T} - \frac{m\eta^2}{2IT} \right]. \quad (A1)$$

The transformation matrix reads

$$\mathbf{M} = (M_{1i}, M_{1i}, \dots, M_{30i})^T, \quad (A2)$$

with elements $M_{1i} = 1, M_{2i} = v_{ix}, M_{3i} = v_{iy}, M_{4i} = v_{iz}, M_{5i} = v_{ix}^2 + v_{iy}^2 + v_{iz}^2 + \eta_i^2, M_{6i} = v_{ix}v_{ix}, M_{7i} = v_{iy}v_{iy}, M_{8i} = v_{iz}v_{iz}, M_{9i} = v_{ix}v_{iy}, M_{10i} = v_{ix}v_{iz}, M_{11i} = v_{iy}v_{iz}, M_{12i} = (v_{ix}^2 + v_{iy}^2 + v_{iz}^2 + \eta_i^2)v_{ix}, M_{13i} = (v_{ix}^2 + v_{iy}^2 + v_{iz}^2 + \eta_i^2)v_{iy}, M_{14i} = (v_{ix}^2 + v_{iy}^2 + v_{iz}^2 + \eta_i^2)v_{iz}, M_{15i} = v_{ix}v_{ix}v_{ix}, M_{16i} = v_{ix}v_{ix}v_{iy}, M_{17i} = v_{ix}v_{ix}v_{iz}, M_{18i} = v_{ix}v_{iy}v_{iy}, M_{19i} = v_{ix}v_{iy}v_{iz}, M_{20i} = v_{ix}v_{iz}v_{iz}, M_{21i} = v_{iy}v_{iy}v_{iy}, M_{22i} = v_{iy}v_{iy}v_{iz}, M_{23i} = v_{iy}v_{iz}v_{iz}, M_{24i} = v_{iz}v_{iz}v_{iz}, M_{25i} = (v_{ix}^2 + v_{iy}^2 + v_{iz}^2 + \eta_i^2)v_{ix}v_{ix}, M_{26i} = (v_{ix}^2 + v_{iy}^2 + v_{iz}^2 + \eta_i^2)v_{ix}v_{iy}, M_{27i} = (v_{ix}^2 + v_{iy}^2 + v_{iz}^2 + \eta_i^2)v_{ix}v_{iz}, M_{28i} = (v_{ix}^2 + v_{iy}^2 + v_{iz}^2 + \eta_i^2)v_{iy}v_{iy}, M_{29i} = (v_{ix}^2 + v_{iy}^2 + v_{iz}^2 + \eta_i^2)v_{iy}v_{iz}, and $M_{30i} = (v_{ix}^2 + v_{iy}^2 + v_{iz}^2 + \eta_i^2)v_{iz}v_{iz}$.$

According to Eq. (3), the kinetic moments of the discrete equilibrium distribution function take the following forms:

$$\hat{f}^{eq} = (\hat{f}_1^{eq}, \hat{f}_2^{eq}, \dots, \hat{f}_{30}^{eq})^T, \quad (A3)$$

with elements $\hat{f}_1^{eq} = \rho, \hat{f}_2^{eq} = \rho u_x, \hat{f}_3^{eq} = \rho u_y, \hat{f}_4^{eq} = \rho u_z, \hat{f}_5^{eq} = \rho[(D+I)T + u^2], \hat{f}_6^{eq} = \rho(T + u_x^2), \hat{f}_7^{eq} = \rho(T + u_y^2), \hat{f}_8^{eq} = \rho(T + u_z^2), \hat{f}_9^{eq} = \rho u_x u_y, \hat{f}_{10}^{eq} = \rho u_x u_z, \hat{f}_{11}^{eq} = \rho u_y u_z, \hat{f}_{12}^{eq} = \rho u_x[(D+I+2)T + u^2], \hat{f}_{13}^{eq} = \rho u_y[(D+I+2)T + u^2], \hat{f}_{14}^{eq} = \rho u_z[(D+I+2)T + u^2], \hat{f}_{15}^{eq} = \rho(3u_x T + u_x^3), \hat{f}_{16}^{eq} = \rho(u_y T + u_x^2 u_y), \hat{f}_{17}^{eq} = \rho(u_z T + u_x^2 u_z), \hat{f}_{18}^{eq} = \rho(u_x T + u_x u_y^2), \hat{f}_{19}^{eq} = \rho u_x u_y u_z, \hat{f}_{20}^{eq} = \rho(u_x T + u_x u_z^2), \hat{f}_{21}^{eq} = \rho(3u_y T + u_y^3), \hat{f}_{22}^{eq} = \rho(u_z T + u_z u_y^2), \hat{f}_{23}^{eq} = \rho(u_y T + u_y u_z^2), \hat{f}_{24}^{eq} = \rho(3u_z T + u_z^3),$

$\hat{f}_{25}^{eq} = \rho T[(D+I+2)T+u^2] + \rho u_x^2[(D+I+4)T+u^2]$, $\hat{f}_{26}^{eq} = \rho u_x u_y[(D+I+4)T+u^2]$, $\hat{f}_{27}^{eq} = \rho u_x u_z[(D+I+4)T+u^2]$, $\hat{f}_{28}^{eq} = \rho T[(D+I+2)T+u^2] + \rho u_y^2[(D+I+4)T+u^2]$, $\hat{f}_{29}^{eq} = \rho u_y u_z[(D+I+4)T+u^2]$, and $\hat{f}_{30}^{eq} = \rho T[(D+I+2)T+u^2] + \rho u_z^2[(D+I+4)T+u^2]$.

The force term reads

$$\hat{F} = (\hat{F}_1, \hat{F}_2, \dots, \hat{F}_{30})^\top, \quad (\text{A4})$$

with elements $\hat{F}_1 = 0$, $\hat{F}_2 = \rho a_x$, $\hat{F}_3 = \rho a_y$, $\hat{F}_4 = \rho a_z$, $\hat{F}_5 = 2\rho(u_x a_x + u_y a_y + u_z a_z)$, $\hat{F}_6 = 2\rho u_x a_x$, $\hat{F}_7 = 2\rho u_y a_y$, $\hat{F}_8 = 2\rho u_z a_z$, $\hat{F}_9 = \rho(u_x a_y + u_y a_x)$, $\hat{F}_{10} = \rho(u_x a_z + u_z a_x)$, $\hat{F}_{11} = \rho(u_y a_z + u_z a_y)$, $\hat{F}_{12} = 2\rho u_x(u_x a_x + u_y a_y + u_z a_z) + \rho a_x[(D+I+2)T+u^2]$, $\hat{F}_{13} = 2\rho u_y(u_x a_x + u_y a_y + u_z a_z) + \rho a_y[(D+I+2)T+u^2]$, $\hat{F}_{14} = 2\rho u_z(u_x a_x + u_y a_y + u_z a_z) + \rho a_z[(D+I+2)T+u^2]$, $\hat{F}_{15} = 3\rho a_x(T+u_x^2)$, $\hat{F}_{16} = \rho[a_y(T+u_x^2) + 2a_x u_x u_y]$, $\hat{F}_{17} = \rho[a_z(T+u_x^2) + 2a_x u_x u_z]$, $\hat{F}_{18} = \rho[a_x(T+u_y^2) + 2a_y u_x u_y]$, $\hat{F}_{19} = \rho[a_x u_x u_z + a_y u_x u_z + a_z u_y u_x]$, $\hat{F}_{20} = \rho[a_x(T+u_z^2) + 2a_z u_x u_z]$, $\hat{F}_{21} = 3\rho a_y(T+u_y^2)$, $\hat{F}_{22} = \rho[a_z(T+u_y^2) + 2a_y u_y u_z]$, $\hat{F}_{23} = \rho[a_y(T+u_z^2) + 2a_z u_y u_z]$, $\hat{F}_{24} = 3\rho a_z(T+u_z^2)$, $\hat{F}_{25} = 2\rho(u_x a_x + u_y a_y + u_z a_z)(T+u_x^2) + 2\rho u_x a_x[(D+I+4)T+u^2]$, $\hat{F}_{26} = 2\rho(u_x a_x + u_y a_y + u_z a_z)u_x u_y + \rho(u_x a_y + u_y a_x)[(D+I+4)T+u^2]$, $\hat{F}_{27} = 2\rho(u_x a_x + u_y a_y + u_z a_z)u_x u_z + \rho(u_x a_z + u_z a_x)[(D+I+4)T+u^2]$, $\hat{F}_{28} = 2\rho(u_x a_x + u_y a_y + u_z a_z)(T+u_y^2) + 2\rho u_y a_y[(D+I+4)T+u^2]$, $\hat{F}_{29} = 2\rho(u_x a_x + u_y a_y + u_z a_z)u_y u_z + \rho(u_y a_z + u_z a_y)[(D+I+4)T+u^2]$, and $\hat{F}_{30} = 2\rho(u_x a_x + u_y a_y + u_z a_z)(T+u_z^2) + 2\rho u_z a_z[(D+I+4)T+u^2]$.

The reaction term is

$$\hat{R} = (\hat{R}_1, \hat{R}_2, \dots, \hat{R}_{30})^\top, \quad (\text{A5})$$

with elements $\hat{R}_1 = 0$, $\hat{R}_2 = 0$, $\hat{R}_3 = 0$, $\hat{R}_4 = 0$, $\hat{R}_5 = (D+I)\rho T'$, $\hat{R}_6 = \rho T'$, $\hat{R}_7 = \rho T'$, $\hat{R}_8 = \rho T'$, $\hat{R}_9 = 0$, $\hat{R}_{10} = 0$, $\hat{R}_{11} = 0$, $\hat{R}_{12} = (D+I+2)\rho u_x T'$, $\hat{R}_{13} = (D+I+2)\rho u_y T'$, $\hat{R}_{14} = (D+I+2)\rho u_z T'$, $\hat{R}_{15} = 3\rho u_x T'$, $\hat{R}_{16} = \rho u_y T'$, $\hat{R}_{17} = \rho u_z T'$, $\hat{R}_{18} = \rho u_x T'$, $\hat{R}_{19} = 0$, $\hat{R}_{20} = \rho u_x T'$, $\hat{R}_{21} = 3\rho u_y T'$, $\hat{R}_{22} = \rho u_z T'$, $\hat{R}_{23} = \rho u_y T'$, $\hat{R}_{24} = 3\rho u_z T'$, $\hat{R}_{25} = [2(D+I+2)T+u^2 + (D+I+4)u_x^2]\rho T'$, $\hat{R}_{26} = \rho T' u_x u_y (D+I+4)$, $\hat{R}_{27} = \rho T' u_x u_z (D+I+4)$, $\hat{R}_{28} = [2(D+I+2)T+u^2 + (D+I+4)u_y^2]\rho T'$, $\hat{R}_{29} = \rho T' u_y u_z (D+I+4)$, and $\hat{R}_{30} = [2(D+I+2)T+u^2 + (D+I+4)u_z^2]\rho T'$.

DATA AVAILABILITY

The data that support the findings of this study are available from the corresponding author upon reasonable request.

REFERENCES

- C. K. Law, *Combustion Physics* (Cambridge University Press, Cambridge, 2006).
- See <https://yearbook.enerdata.net/total-energy/world-consumption-statistics.html> for trend over 1990–2019, in global energy statistical yearbook 2020.
- E. Nagnibeda and E. Kustova, *Non-Equilibrium Reacting Gas Flows: Kinetic Theory of Transport and Relaxation Processes* (Springer, Berlin, 2009).
- E. V. Kustova and D. Giordano, "Cross-coupling effects in chemically non-equilibrium viscous compressible flows," *Chem. Phys.* **379**, 83–91 (2011).

- A. Munafò, M. Panesi, and T. E. Magin, "Boltzmann rovibrational collisional coarse-grained model for internal energy excitation and dissociation in hypersonic flows," *Phys. Rev. E* **89**, 023001 (2014).
- Y. Ju, "Recent progress and challenges in fundamental combustion research," *Adv. Appl. Mech.* **44**, 201402 (2014).
- N. Gebbeken, S. Greulich, and A. Pietzsch, "Hugoniot properties for concrete determined by full-scale detonation experiments and flyer-plate-impact tests," *Int. J. Impact Eng.* **32**, 2017–2031 (2006).
- J. A. T. Gray, M. Lemke, J. Reiss, C. O. Paschereit, J. Sesterhenn, and J. P. Moeck, "A compact shock-focusing geometry for detonation initiation: Experiments and adjoint-based variational data assimilation," *Combust. Flame* **183**, 144–156 (2017).
- S. T. Parete-Koon, C. R. Smith, T. L. Papatheodore, and O. E. Bronson Messer, "A review of direct numerical simulations of astrophysical detonations and their implications," *Front. Phys.* **8**, 189–198 (2013).
- Y. Mahmoudi, N. Karimi, R. Deiterding, and S. Emami, "Hydrodynamic instabilities in gaseous detonations: Comparison of Euler, Navier–Stokes, and large-eddy simulation," *J. Propul. Power* **30**, 384–396 (2014).
- B. M. Haines, F. F. Grinstein, and J. D. Schwarzkopf, "Reynolds-averaged Navier–Stokes initialization and benchmarking in shock-driven turbulent mixing," *J. Turbul.* **14**, 46–70 (2013).
- Y. Zhang, R. Qin, and D. R. Emerson, "Lattice Boltzmann simulation of rarefied gas flows in microchannels," *Phys. Rev. E* **71**, 047702 (2005).
- J. Meng, Y. Zhang, N. G. Hadjiconstantinou, G. A. Radtke, and X. Shan, "Lattice ellipsoidal statistical BGK model for thermal non-equilibrium flows," *J. Fluid Mech.* **718**, 347–370 (2013).
- V. V. Zhakhovskii, K. Nishihara, and S. I. Anisimov, "Shock wave structure in dense gases," *JETP Lett.* **66**, 99–105 (1997).
- B. L. Holian, C. W. Patterson, M. Mareschal, and E. Salomons, "Modeling shock waves in an ideal gas: Going beyond the Navier–Stokes level," *Phys. Rev. E* **47**, R24–R27 (1993).
- B. L. Holian and M. Mareschal, "Heat-flow equation motivated by the ideal-gas shock wave," *Phys. Rev. E* **82**, 026707 (2010).
- A. V. Bobylev, M. Bisi, M. P. Cassinari, and G. Spiga, "Shock wave structure for generalized Burnett equations," *Phys. Fluids* **23**, 030607 (2011).
- S. Succi, *The Lattice Boltzmann Equation: For Complex States of Flowing Matter* (Oxford University Press, 2018).
- S. Succi, G. Bella, and F. Papetti, "Lattice kinetic theory for numerical combustion," *J. Sci. Comput.* **12**, 395–408 (1997).
- O. Filippova and D. Hänel, "A novel lattice BGK approach for low Mach number combustion," *J. Comput. Phys.* **158**, 139–160 (2000).
- O. Filippova and D. Hänel, "A novel numerical scheme for reactive flows at low Mach numbers," *Comput. Phys. Commun.* **129**, 267–274 (2000).
- S. A. Hosseini, A. Eshghinejadfard, N. Darabiha, and D. Thévenin, "Weakly compressible lattice Boltzmann simulations of reacting flows with detailed thermo-chemical models," *Comput. Math. Appl.* **79**, 141–158 (2020).
- S. A. Hosseini, H. Safari, N. Darabiha, D. Thévenin, and M. Krafczyk, "Hybrid lattice Boltzmann-finite difference model for low Mach number combustion simulation," *Combust. Flame* **209**, 394–404 (2019).
- Y. Peng, C. Shu, and Y. T. Chew, "Simplified thermal lattice Boltzmann model for incompressible thermal flows," *Phys. Rev. E* **68**, 026701 (2003).
- K. Yamamoto, X. He, and G. D. Doolen, "Simulation of combustion field with lattice Boltzmann method," *J. Stat. Phys.* **107**, 367–383 (2002).
- K. Yamamoto, "LB simulation on combustion with turbulence," *Int. J. Mod. Phys. B* **17**, 197–200 (2008).
- T. Lee, C. Lin, and L. Chen, "A lattice Boltzmann algorithm for calculation of the laminar jet diffusion flame," *J. Comput. Phys.* **215**, 133–152 (2006).
- S. Chen, Z. Liu, C. Zhang, Z. He, Z. Tian, B. Shi, and C. Zheng, "A novel coupled lattice Boltzmann model for low Mach number combustion simulation," *Appl. Math. Comput.* **193**, 266–284 (2007).
- S. Chen, Z. Liu, Z. Tian, B. Shi, and C. Zheng, "A simple lattice Boltzmann scheme for combustion simulation," *Comput. Math. Appl.* **55**, 1424–1432 (2008).
- A. F. di Rienzo, P. Asinari, E. Chiavazzo, N. I. Prasianakis, and J. Mantzaras, "Lattice Boltzmann model for reactive flow simulations," *Europhys. Lett.* **98**, 34001 (2012).

- ³¹B. Yan, A. Xu, G. Zhang, Y. Ying, and H. Li, "Lattice Boltzmann model for combustion and detonation," *Front. Phys.* **8**, 94–110 (2013).
- ³²C. Lin, A. Xu, G. Zhang, and Y. Li, "Polar coordinate lattice Boltzmann kinetic modeling of detonation phenomena," *Commun. Theor. Phys.* **62**, 737–748 (2014).
- ³³A. Xu, C. Lin, G. Zhang, and Y. Li, "Multiple-relaxation-time lattice Boltzmann kinetic model for combustion," *Phys. Rev. E* **91**, 043306 (2015).
- ³⁴C. Lin, A. Xu, G. Zhang, and Y. Li, "Double-distribution-function discrete Boltzmann model for combustion," *Combust. Flame* **164**, 137–151 (2016).
- ³⁵C. Lin and K. H. Luo, "Mesoscopic simulation of nonequilibrium detonation with discrete Boltzmann method," *Combust. Flame* **198**, 356–362 (2018).
- ³⁶C. Lin and K. H. Luo, "Discrete Boltzmann modeling of unsteady reactive flows with nonequilibrium effects," *Phys. Rev. E* **99**, 012142 (2019).
- ³⁷T. Yang, J. Wang, L. Yang, and C. Shu, "Development of multi-component generalized sphere function based gas-kinetic flux solver for simulation of compressible viscous reacting flows," *Comput. Fluids* **197**, 104382 (2020).
- ³⁸S. Ansumali and I. V. Karlin, "Consistent lattice Boltzmann method," *Phys. Rev. Lett.* **95**, 260605 (2005).
- ³⁹C. Lin and K. H. Luo, "MRT discrete Boltzmann method for compressible exothermic reactive flows," *Comput. Fluids* **166**, 176–183 (2018).
- ⁴⁰T. Ruggeri and M. Sugiyama, *Rational Extended Thermodynamics Beyond the Monatomic Gas* (Springer, 2015).
- ⁴¹T. Ruggeri, "Maximum entropy principle closure for 14-moment system for a non-polytropic gas," *Ric. Mat.* **2020**, 1–16.
- ⁴²Y. Gan, A. Xu, G. Zhang, and H. Lai, "Three-dimensional discrete Boltzmann models for compressible flows in and out of equilibrium," *Proc. Inst. Mech. Eng., Part C* **232**, 477–490 (2018).
- ⁴³S. Chen, H. Chen, D. Martnez, and W. Matthaeus, "Lattice Boltzmann model for simulation of magnetohydrodynamics," *Phys. Rev. Lett.* **67**, 3776 (1991).
- ⁴⁴Y. H. Qian, D. D'Humières, and P. Lallemand, "Lattice BGK models for Navier–Stokes equation," *Europhys. Lett.* **17**, 479 (1992).
- ⁴⁵J. Bourgat, L. Desvillettes, P. Tallec, and B. Perthame, "Microreversible collisions for polyatomic gases and Boltzmann's theorem," *Eur. J. Mech. B* **13**, 237–254 (1994).
- ⁴⁶H. Lai, A. Xu, G. Zhang, Y. Gan, Y. Ying, and S. Succi, "Non-equilibrium thermo-hydrodynamic effects on the Rayleigh-Taylor instability in compressible flows," *Phys. Rev. E* **94**, 023106 (2016).
- ⁴⁷T. Kataoka and M. Tsutahara, "Lattice Boltzmann model for the compressible Navier-Stokes equations with flexible specific-heat ratio," *Phys. Rev. E* **69**, 35701 (2004).
- ⁴⁸M. Watari and M. Tsutahara, "Two-dimensional thermal model of the finite-difference lattice Boltzmann method with high spatial isotropy," *Phys. Rev. E* **67**, 036306 (2003).
- ⁴⁹M. Watari, "Is the lattice Boltzmann method applicable to rarefied gas flows? Comprehensive evaluation of the higher-order models," *J. Fluids Eng.* **138**, 011202 (2016).
- ⁵⁰F. Chen, A. Xu, G. Zhang, Y. Li, and S. Succi, "Multiple-relaxation-time lattice Boltzmann approach to compressible flows with flexible specific-heat ratio and Prandtl number," *Europhys. Lett.* **90**, 54003 (2010).
- ⁵¹Y. Zhang, A. Xu, G. Zhang, C. Zhu, and C. Lin, "Kinetic modeling of detonation and effects of negative temperature coefficient," *Combust. Flame* **173**, 483–492 (2016).
- ⁵²C. Shu and S. Osher, "Efficient implementation of essentially non-oscillatory shock-capturing schemes," *J. Comput. Phys.* **77**, 439–471 (1989).
- ⁵³H. D. Ng, M. I. Radulescu, A. J. Higgins, N. Nikiforakis, and J. H. S. Lee, "Numerical investigation of the instability for one-dimensional Chapman–Jouguet detonations with chain-branching kinetics," *Combust. Theory Modell.* **9**, 385–401 (2005).
- ⁵⁴W. Fickett and W. W. Wood, "Flow calculations for pulsating one-dimensional detonations," *Phys. Fluids* **9**, 903–916 (1966).
- ⁵⁵H. I. Lee and D. S. Stewart, "Calculation of linear detonation instability: One-dimensional instability of planer detonations," *J. Fluid Mech.* **216**, 103–132 (1990).
- ⁵⁶A. Bourlioux and A. J. Majda, "Theoretical and numerical structure for unstable one-dimensional detonations," *Combust. Flame* **90**, 211–229 (1992).
- ⁵⁷Z. Gao, W. Don, and Z. Li, "High order weighted essentially non-oscillation schemes for one-dimensional detonation wave simulations," *J. Comput. Math.* **29**, 623 (2011).
- ⁵⁸C. Wang, P. Li, Z. Gao, and W. Don, "Three-dimensional detonation simulations with the mapped WENO-Z finite difference scheme," *Comput. Fluids* **139**, 105–111 (2016).